

WHAT LURKS IN THE MARTIAN ROCKS AND SOIL? INVESTIGATIONS OF SULFATES, PHOSPHATES, AND PERCHLORATES

Optical constants of synthetic potassium, sodium, and hydronium jarosite†

ELIZABETH C. SKLUTE^{1,*}, TIMOTHY D. GLOTCH¹, JENNIFER L. PIATEK², WILLIAM R. WOERNER¹,
ALEXIS A. MARTONE¹ AND MEREDITH L. KRANER¹

¹Department of Geosciences, Stony Brook University, Stony Brook, New York 11794, U.S.A.

²Department of Physics and Earth Sciences, Central Connecticut State University, New Britain, Connecticut 06050, U.S.A.

ABSTRACT

The hydroxy sulfate jarosite $[(K,Na,H_3O)Fe_3(SO_4)_2(OH)_6]$ has both been discovered on Mars, and is associated with areas of highly acidic runoff on Earth. Because jarosite is extremely sensitive to formation conditions, it is an important target mineral for remote sensing applications. Yet at visible and near infrared (VNIR) wavelengths, where many spacecraft spectrometers collect data, the spectral abundance of a mineral in a mixture is not linearly correlated with the surface abundance of that mineral. Radiative transfer modeling can be used to extract quantitative abundance estimates if the optical constants (the real and imaginary indices of refraction, n and k) for all minerals in the mixture are known. Unfortunately, optical constants for a wide variety of minerals, including sulfates like jarosite, are not available. This is due, in part, to the inherent difficulty in obtaining such data for minerals that tend to crystallize naturally as fine-grained ($\sim 10 \mu\text{m}$) powders, like many sulfates including jarosite. However, the optical constants of powders can be obtained by inverting the equation of radiative transfer and using it to model laboratory spectra. In this paper, we provide robust n and k data for synthetic potassium, hydronium, and sodium jarosite in the VNIR. We also explicitly describe the calculation procedures (including access to our Matlab code) so that others may obtain optical constants of additional minerals. Expansion of the optical constants library in the VNIR will facilitate the extraction of quantitative mineral abundances, leading to more in-depth evaluations of remote sensing target locations.

Keywords: Jarosite, optical constants, radiative transfer, Hapke, index of refraction, sulfate, Mars, AMD

INTRODUCTION

Jarosite has been the subject of a multitude of studies over the past decade (Bishop and Murad 2005; Frost et al. 2005; Navrotsky et al. 2005; Nomura et al. 2005; Barron et al. 2006; Papike et al. 2007; Cloutis et al. 2008; Madden et al. 2008, 2012; Bell et al. 2010; Norlund et al. 2010; Kula and Baldwin 2011; Pritchett et al. 2012; Zahrai et al. 2013) since its discovery on Mars in 2004 at the Mars Exploration Rover Opportunity landing site at Meridiani Planum (Klingelhofer et al. 2004). On Earth, this iron hydroxy sulfate $[(K,Na,H_3O)Fe_3(SO_4)_2(OH)_6]$ occurs primarily as an oxidative weathering product of pyrite-rich sediments associated with acid mine drainage (AMD) (Navrotsky et al. 2005). Therefore, its discovery on Mars suggests a highly acidic formation environment (Bishop et al. 2004). On both Earth and Mars, jarosite's sensitivity to formation conditions makes it an important environmental indicator. It is, therefore, a key remote sensing target. Visible and near infrared (VNIR) remote sensing has been used to identify and map jarosite on both planets (Swayze et al. 2000; Farrand et al. 2009). However, quantitative abundance estimates cannot be extracted from these data because of a lack of optical constants (the real and imaginary indices of

refraction, n and k). The absence of these optical constants from the literature is due, in part, to the inherent difficulty in obtaining such data for minerals that tend to crystallize naturally as fine-grained ($\sim 10 \mu\text{m}$) powders, like many sulfates including jarosite. Yet once optical constants have been determined, and quantitative mineral abundances obtained, it becomes possible to conduct a more in-depth evaluation of the target location.

As additional jarosite-bearing regions are discovered on Mars (Farrand et al. 2009; Roach et al. 2010; Wendt et al. 2011; Sefton-Nash et al. 2012; Sowe et al. 2012), there is a growing need for tools and data that can enhance our interpretations of past martian environments. In the absence of targeted sample return, quantitatively modeled mineral abundances derived from remote sensing data can provide valuable constraints on past fluid compositions, atmospheric conditions, weathering timelines, and sub-surface processes. This will aid in developing a full picture of martian history. To this end, jarosite is a particularly valuable environmental indicator mineral because it is extremely sensitive to environmental conditions. For example, terrestrial jarosite only precipitates under very specific Eh and pH conditions as a supergene deposit (Bigham et al. 1996a, 1996b; Norlund et al. 2010). It also only remains stable under a narrow range of atmospheric and surface conditions (i.e., low surface moisture and low relative humidity (Madden et al. 2004; Papike et al. 2006)). This sensitivity has allowed it to be used as a "stopwatch" for wetting processes on Mars (Madden et al. 2009). Jarosite can

* E-mail: elizabeth.sklute@gmail.com

† Special collection papers can be found on GSW at <http://ammin.geoscienceworld.org/site/misc/specialissuelist.xhtml>.

also crystallize from subsurface (volcanic) processes, and its ability to easily incorporate rare earth elements into its structure makes it a valuable geochronometer (Lueth et al. 2005; Papike et al. 2006). Jarosite can also be used as a geothermometer both through oxygen isotopes analysis (Rye and Stoffregen 1995; Papike et al. 2006) and hydronium content (Swayze et al. 2008). In addition, because jarosite is a well-studied mineral, thermodynamic data are available to model its formation, stability, and partitioning behavior (Drouet and Navrotsky 2003; Navrotsky et al. 2005). For example, it is possible to determine the K/Na ratio of the fluid from which jarosite formed (Deyell and Dipple 2005; Papike et al. 2006).

On Earth, jarosite is quickly becoming a major environmental contaminant (Pappu et al. 2006). As one of the main byproducts of hydrometallurgical extraction of zinc (600 000 barrels of residue annually in the European Union), and as a precipitate linked to highly acidic AMD runoff (Swayze et al. 2000), it has the capacity to both store and release large quantities of heavy metals back into the environment (Papike et al. 2006; Swayze et al. 2008). In AMD regions, the most acidic runoffs are associated with Fe(III) sulfates (Jerz and Rimstidt 2003). Among these, jarosite is often spectrally significant on remote sensing spatial scales. It indicates areas where neutral rain and snow melt can be transformed into pH <3 runoff (Swayze et al. 2000; Jerz and Rimstidt 2003). Swayze et al. (2000) showed that identifying jarosite in remote spectral analysis of AMD regions saved both time (2 years) and money (\$2 million) in cleanup efforts at the California Gulch Superfund site in Leadville, Colorado, compared to traditional remediation methods.

For single pass or targeted cleanup efforts, qualitative data may be sufficient. However, for monitoring, quantitatively determined abundances would greatly improve efficiency. As aeolian processes expose more pyrite to oxygen and water, jarosite concentrations increase, indicating an active area of contamination. If, however, an AMD region is no longer producing highly acidic waters, conditions will favor the formation of goethite and hematite, causing jarosite concentrations to diminish with time. Thus, by combining quantitative abundance analysis with the broad spatial coverage of remote sensing, detailed geochemical conditions on the ground can be assessed in a manner that broadens scope and significantly reduces time and cost.

Jarosite is spectrally distinct in the VNIR (~0.35–2.5 μm) wavelength range from other hydrates, hydroxylates, and iron-bearing minerals (Fig. 1; Swayze et al. 2000). On a remote sensing platform, VNIR spectroscopy remains one of the most useful methods for identifying hydrated and hydroxylated minerals, like jarosite, over large spatial scales. This technique is, therefore, an indispensable tool for wide-scale monitoring and discovery missions. While VNIR spectroscopic identification of many minerals is straightforward (Clark et al. 2003), extracting quantitative abundances of single minerals from spectra of mineral mixtures can be quite difficult. In this wavelength region, multiple scattering is often the dominant process, in contrast to the mid-infrared (MIR), where absorption dominates (Clark 1999). The dominant scattering condition in the VNIR, which impacts the shape and depth of spectral features, depends on grain size, absorption coefficient, and internal and surface imperfections. In addition, light can be scattered multiple times

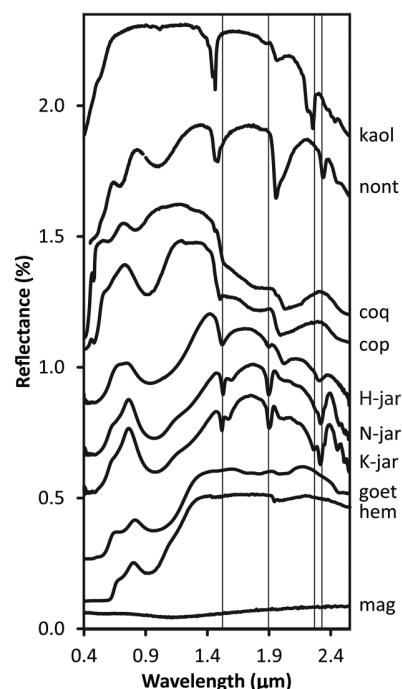


FIGURE 1. VNIR spectra of several common minerals (USGS SpecLab) plotted with the jarosites used in this study. Abbreviations are as follows: kaolinite CM7 (kaol), nontronite NG-1.a (nont), coquimbite GDS22 (coq), copiapite GDS21 (cop), hydronium jarosite 63–90 μm (H-jar), sodium jarosite 63–90 μm (N-jar), potassium jarosite 63–90 μm (K-jar), goethite GDS134 (goet), hematite GDS27 (hem), magnetite HS195.3B (mag). Vertical lines mark the diagnostic jarosite spectral features.

in a regolith surface before being absorbed or reflected to a detector. This means that the contribution to a spectrum from a mineral in a mixture is not necessarily linearly correlated with its abundance in the sample (Hapke and Wells 1981). Therefore, a model is needed to relate the spectral abundance of a mineral with its abundance in a mineral mixture.

Fortunately, radiative transfer theory can be used to tackle the problem of nonlinear spectral mixing and to extract quantitative mineral abundance in the VNIR (Clark and Roush 1984; Mustard and Pieters 1987; Lucey 2004; Poulet and Erard 2004; Wilcox et al. 2006; Cahill and Lucey 2007; Lawrence and Lucey 2007; Denevi et al. 2008; Cahill et al. 2009; Poulet et al. 2009; Li and Li 2011). Quantitative abundances are obtainable because radiative transfer theory explicitly models the interaction of light with particles, like atmospheric dust and aerosols, or soils and regoliths. Unmixing models based on radiative transfer theory use the fact that although reflectance is not linearly correlated with concentration in a mixed spectrum, the bulk single scattering albedo (SSA), or the probability that a photon will survive the interaction with a particle, is a linear combination of the SSA's of the minerals in the mixture. The SSA can be obtained from VNIR reflectance data, provided that the real and imaginary indices of refraction (optical constants n and k), of the minerals in the mixture are known and an effective particle size of the target can be estimated. However, this method has seen limited use due to a distinct lack of optical constants for a wide variety of materi-

als (Lucey 1998; Dalton et al. 2004; Cruikshank et al. 2005).

Optical constants can be determined by various methods provided that large (millimeter-) sized crystals of the pure material can be grown. For naturally fine-grained minerals (like many sulfates) that cannot be cast into thin films, optical constants can only be determined through inverting the theory of radiative transfer and applying it to spectra of pure minerals obtained in the lab. Although several treatments of radiative transfer theory, developed in the 1980s by Hapke (Hapke 1981, 1993), and later in the 1990s/2000s by Shkuratov et al. (1999), made this procedure more computationally straightforward, it remained, until recently, a lengthy and user intensive process. Recent increases in computing power have made the calculation of optical constants more robust and less time consuming. However, a general lack of detailed methodology in the literature for these more robust methods has hindered potential progress. Here we contribute to the library of optical constants in two ways: first, by providing robust n and k data for synthetic potassium, hydronium, and sodium jarosite; and second, by explicitly describing the calculation procedures, providing our Matlab computer code, and detailing how others may obtain optical constants of additional minerals.

METHOD

Sample synthesis

We synthesized hydronium jarosite following a modified method from Majzlan et al. (2004). Hydrothermal reactions were carried out in 23 mL polytetrafluoroethylene-lined Parr pressure vessels. Each liner was filled with a mix of 12 mL of 18 m Ω millipore DI water and 3 g of Fe₂(SO₄)₃ · 5 H₂O and magnetically stirred for 30 min. The vessels were sealed and placed in a Fisher Isotemp forced-air circulation oven at 142 °C for 48 h. After the reaction, the hydronium jarosite was washed with DI water and dried in an oven at 40 °C for 12 h. The products of 16 reactions were combined for this study.

Potassium and sodium jarosite were synthesized following the redox-based hydrothermal method of Grohol et al. (2003). The 23 mL polytetrafluoroethylene-lined Parr pressure vessels were first loaded with 9.2 mL of 18 m Ω millipore DI water, 0.405 mL of H₂SO₄, and 0.9 g of K₂SO₄ for potassium jarosite or 0.626 g of Na₂SO₄ in the case of sodium jarosite. The solutions were magnetically stirred for 30 min then placed in a glove bag with an O₂ atmosphere. A 0.103 g piece of 2 mm diameter iron wire (99.9% Aldrich), was added to the solution. The pressure vessels were sealed with an oxygen atmosphere. Prior to being added to the polytetrafluoroethylene vessels, the iron wire was cleaned of any surface oxide residue by heating it to 800 °C under an H₂ atmosphere for 1 h. The pressure vessels were then placed in a Fisher Isotemp forced-air circulation oven at 201 °C for 4 days. After the reaction, the products were washed in DI water and dried in an oven at 40 °C for 12 h. For potassium jarosite, the largest grain sizes were obtained when the Parr autoclaves were cooled at 0.1 °C/min. For the sodium jarosites, large grain sizes required seeding from previous batches, and best results were obtained when the autoclaves were pulled directly from the oven after 4 days. For potassium and sodium jarosite, the products of 32 and 16 reactions, respectively, were combined for this study.

Analysis

The synthesis products were dry-sieved into four size fractions: <45, 45–63, 63–90, and 90–125 μ m. Powder XRD patterns were collected using a Rigaku Ultima IV diffractometer (CuK α) in Bragg-Brentano reflection geometry with a D/teX Ultra high-speed one-dimensional position sensitive detector. The patterns were collected from 10 to 159° at a rate of 0.5 °/min with a 0.01° step size for phase identification. Reflectance spectra of the three largest size fractions were collected using an 8° field of view foreoptic lens coupled via an optical fiber to an ASD Fieldspec3 Max UV-VIS-NIR spectrometer with a 512 element Si photodiode array detector for the 350–1000 nm interval and two TE cooled InGaAs photodiode detectors in the 1000–2500 nm interval, giving spectral resolution of 10 nm (at 1400 or 2100 nm). The incident light was provided by an Ocean Optics HL-2000-HP tungsten halogen light source directed down a 600 μ m Ocean Optics optical fiber. Each size fraction of each sample was analyzed at 7 phase angles from 15 to 45° (spectra taken every 5°). Incidence and emergence angles were obtained by using a custom-built goniometer

(estimated error of <2°). All spectra were taken in the absence of ambient light and referenced to a calibrated Spectralon standard (Labsphere, Inc.), illuminated at the same angle as the sample. Since the intensity of the reflectance varied with phase angle, the number of averaged scans was increased as phase angle increased to improve signal to noise. At incidence of 15°, each spectrum is an average of 3000 scans. At 45°, each spectrum is an average of 7500 scans. Due to the changing phase angle, the detector was optimized, and a new white reflectance baseline (500 scans dark current, 1000 scans white reflectance) was acquired before each measurement. Samples were mounted into an XRD sample holder painted flat black. Rather than packing the sample into the sample holder by compression, which can add preferential orientation and possibly introduce coherent effects, each sample was leveled by tapping the sides and underside of the sample plate. Repeat measurements from separate sample loadings of the same sample in the same configuration were compared, and errors were found to be ~0.01% reflectance.

The smallest size fraction of each sample was pressed into a compact pellet ~2 mm thickness and 13 mm diameter. Midinfrared (MIR) and far infrared (FIR) (for potassium jarosite only) specular reflectance spectra were collected for each pellet. MIR measurements were made on a Thermo-Fisher Nicolet 6700 FTIR spectrometer with a DTGS detector (with a KBr window) and a CsI beamsplitter. FIR measurements were made on the same spectrometer equipped with a Nicolet Solid Substrate beamsplitter and a DTGS detector with a polyethylene window. MIR and FIR reflectance spectra were referenced to a gold mirror and each spectrum is an average of 256 scans.

The porosity of each sample was estimated as 1-(bulk density/particle density). Since the grain size ranges are small and approximately equivalent in shape, it was assumed that particles would pack similarly for each grain size range. Therefore, a single value for porosity was used for each sample. However, due to the very small amount of sample available for analysis, the porosity estimates are considered quite rough, thus optical constants are reported with and without a porosity correction.

Theory

The equation of radiative transfer (a form of the Boltzmann transfer equation; Hapke 2012), which explicitly models the interaction of light with a medium, has no analytic closed form solution (Hapke 2012). Therefore, use of the equation of radiative transfer varies based on the exact set of approximations or formulations used to obtain results. There are two primary modern formulations that have been applied to the modeling of planetary bodies: the Hapke model (Hapke 1981, 1996, 2012) and the Shkuratov model (Shkuratov et al. 1999). Although the Shkuratov model has the advantage of computational simplicity, we have found it suffers from two drawbacks. First and foremost, we know that the imaginary index of refraction, k , is a fundamental property of a mineral and is, therefore, grain-size independent. However, the computational simplicity of the Shkuratov model means that the same k cannot be obtained for two different size fractions of the same sample. Thus although a useable, and often useful quantity is obtained, it is not technically correct to call it k . Second, the Shkuratov model ignores illumination and viewing geometry, making it impossible to take factors like surface roughness into account (Li and Li 2011).

For these reasons, our model is based on the Hapke treatment of radiative transfer. The equations used in this work are slightly altered from those in the literature. Our equations follow directly from the theory as it is presented by Hapke. However, we make fewer assumptions about our reflectance experiment, which cause the geometry (placement of μ and μ_0) in some of the expressions to differ from what is traditionally reported in the literature.

The Hapke treatment of radiative transfer requires three things: that the particle size be much greater than the wavelength of light; that the medium be continuous and closely packed such that the particles are touching; and that they are randomly oriented such that the multiply scattered light can be assumed isotropic [see Hapke (2012) for a full derivation and explanation]. If these conditions are met, the bidirectional reflectance, or the ratio of the scattered radiance I to the source irradiance J , is

$$r(i, e, g) = K \frac{w}{4\pi \mu_0 + \mu} \left[\left[1 + B(g) \right] p(g) + H(\mu_0 / K) H(\mu / K) - 1 \right], \quad (1)$$

where μ and μ_0 are the cosine of the emission angle, e , and the incidence angle, i , respectively, and g is the phase angle. In Equation 1, $B(g)$ is the backscatter function, which can be set to zero if the phase angle is >15° (Mustard and Pieters 1989). The phase angle dependence of singly scattered light is represented by $p(g)$, the phase function, and can be modeled with a two term Legendre polynomial, such that

$$p(g) = 1 + bc \cos(g) + c \left[1.5 \cos^2(g) - 0.5 \right]. \quad (2)$$

Multiply scattered light is described by Ambartsumian-Chandrasekhar's H -function (Ambartsumian 1958; Chandrasekhar 1960), which can be approximated by

$$H(x) = \left[1 - wx \left[r_0 + \left(\frac{1 - 2r_0x}{2} \right) \ln \left(\frac{1+x}{x} \right) \right] \right]^{-1}. \quad (3)$$

Here $r_0 = (1 - \gamma)/(1 + \gamma)$ is the diffuse reflectance and $\gamma = \sqrt{1 - w}$ is the albedo factor (Hapke 2002). The variable w is the single scattering albedo (SSA), and for a closely packed medium is

$$w = Q_s = S_e + (1 - S_e) \frac{(1 - S_i)}{1 - S_i \Theta}. \quad (4)$$

In Equation 4, Θ is the internal transmission factor, such that

$$\Theta = \frac{r_i + \exp\left(-\sqrt{\alpha(\alpha + s)} \langle D \rangle\right)}{1 + r_i \exp\left(-\sqrt{\alpha(\alpha + s)} \langle D \rangle\right)}, \quad (5)$$

$\langle D \rangle$ is the effective grain size or the path length traveled by light through a particle, s is the internal scattering factor, and $\alpha = 4\pi k/\lambda$ is the absorption coefficient. In Equation 4, S_i and S_e are the Fresnel reflectance coefficients integrated over all angles and can be approximated by

$$S_i \approx 1.014 - \frac{4}{n(n+1)^2} \quad (7)$$

and

$$S_e \approx \frac{(n-1)^2 + k^2}{(n+1)^2 + k^2} + 0.05. \quad (8)$$

The constant, K , is the porosity factor (Hapke 2008). For equant particles,

$$K = -\ln \frac{(1 - 1.209\phi^{(2/3)})}{1.209\phi^{(2/3)}}, \quad (9)$$

where $\phi = 1 - \text{porosity}$ is the filling factor. Porosity effects can significantly change the reflectance properties of a medium. If porosity effects are not accounted for explicitly, the calculated value of k may be too small by as much as a factor of 2 (Hapke 2012). However, due to a large degree of uncertainty in the value of ϕ , which clearly accounts for the largest source of error in the calculation of k , optical constants are reported both with and without a porosity correction.

Strictly speaking, what is measured in a bidirectional reflectance experiment is not the ratio of the radiance to the irradiance, I/J , as is the definition of Equation 1, but the radiance I . The following derivation is adapted from Piatek (2003).

Let the area of the sample illuminated by the source be Ab . When the source is not normal to the sample, the illuminated area will be stretched by incidence angle μ_0 , such that $I = J \cdot Ab/\mu_0$. Similarly, if the detector, which can be assumed to be sensitive only to light from the source (even if it "sees" a greater area of the sample) is not normal to the sample, it will "see" an area that is stretched by emission angle μ , such that $I = J \cdot r(i, e, g) \cdot \mu$. Combining terms, you get

$$I(i, e, g) = J \cdot \frac{Ab}{\mu_0} \cdot \mu \cdot r(i, e, g) = JAb \cdot \frac{\mu}{\mu_0} \cdot r(i, e, g). \quad (10)$$

The term JAb cannot be explicitly calculated. However, in a bidirectional reflectance experiment, each measurement is referenced to a standard. The same procedure would show that the radiance of the standard is

$$I(i', e', g') = JAb \cdot \frac{\mu'}{\mu'_0} \cdot r(i', e', g'). \quad (11)$$

The quantity actually recorded by the spectrometer is then

$$\frac{I(i, e, g)}{I(i', e', g')} = \frac{\frac{\mu}{\mu_0} \cdot r(i, e, g)}{\frac{\mu'}{\mu'_0} \cdot r(i', e', g')}. \quad (12)$$

Here we have to make a choice of how to deal with the standard. A primary assumption in the literature (Mustard and Pieters 1987; Lucey 2004; Dalton and Pitman 2012) is that commercially available calibrated Spectralon standards are Lambertian scatterers. Although this may be true for hemispherical reflectance experiments (the calibration file for Spectralon is in hemispherical reflectance), it is not true for bidirectional reflectance (Fig. 2; Piatek 2003). Therefore, the standard is treated as an isotropic scatterer, i.e., setting $p(g) = 1$. Now, substituting in values for r and r' , and still assuming that $B(g) = 0$, we get

$$\frac{I(i, e, g)}{I(i', e', g')} = \frac{\frac{\mu}{\mu_0} \left[K \frac{w}{4\pi \mu_0 + \mu} (p(g) + H(\frac{\mu_0}{K}) H(\frac{\mu}{K}) - 1) \right]}{\frac{\mu'}{\mu'_0} \left[\frac{w'}{4\pi \mu'_0 + \mu'} (H(\mu'_0) H(\mu') - 1) \right]} \quad (13)$$

$$= \frac{\left[K \frac{w}{4\pi \mu_0 + \mu} (p(g) + H(\frac{\mu_0}{K}) H(\frac{\mu}{K}) - 1) \right]}{\left[\frac{w'}{4\pi \mu'_0 + \mu'} (H(\mu'_0) H(\mu') - 1) \right]}. \quad (14)$$

Because the sample was calibrated at each phase angle, $i = i'$ and $e = e'$ for our experiments. However, this is not required should a single calibration be used for multiple measurements.

The single scattering albedo for Spectralon can be quickly determined using the calibration data supplied by the manufacturer and a minimization code in Matlab, since the hemispherical reflectance is simply $r_h = 1 - \gamma H(\mu_0^*)$ (Hapke 2002; Piatek 2003). Equation 14 is the relationship used in all of our programs. The above derivation assumes that ambient light does not contribute to light recorded by the detector. This is a valid assumption for our experiment since spectra are acquired in the absence of ambient light.

Program description

The variables or unknown quantities in the above series of equations are the apparent grain size, $\langle D \rangle$, the internal scattering parameter, s , the phase function coefficients, b and c , and, of course, the wavelength-dependent real and imaginary indices of refraction, n and k . When dealing with a single-phase angle of a single grain-size, the radiative transfer problem is under-determined. However, solving simultaneously for multiple size fractions and/or multiple phase angles results in an over-determined problem, for which all variables can be calculated. The code is split into three routines, which are run iteratively (Fig. 3)—one that determines k from three mineral size fractions, one that determines n from k , and one that calculates appropriate phase function coefficients. The code is split in this way because a too highly over-determined problem can suffer from non-uniqueness of fit.

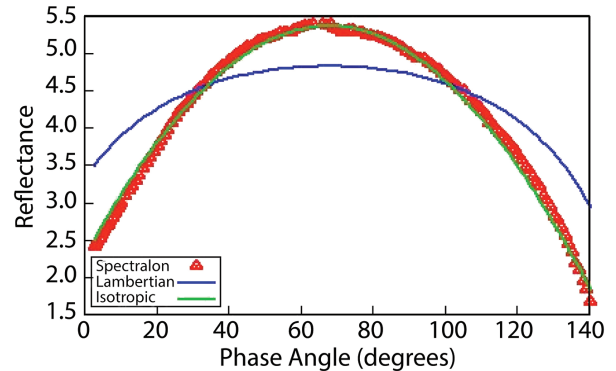


FIGURE 2. Phase curve for Spectralon reflectance standard, taken on a short arm goniometer with an incidence angle of 60°. Reference curves for a Lambertian and an isotropic scatterer show that Spectralon is an isotropic scatterer when used in a bidirectional reflectance experimental setup. Figure reproduced from Piatek (2003). Data are shown as absolute reflectance.

Each VNIR spectrum was smoothed once using a moving average low pass filter and then run through a Matlab encoded program following the method of previous workers (Lucey 1998; Quinn 2010; Quinn et al. 2010). This code first calculates the imaginary index of refraction, k , for each grain size individually, by assuming a constant real index of refraction, n , over the VNIR wavelength range, as well as fixed guesses for b , c , $\langle D \rangle$, and s (initial guesses for b and c were taken from Mustard and Pieters (1989), $\langle D \rangle$ was assumed to be the smallest size in the distribution, and s was initially set to zero). The code then matches the radiance coefficient at each wavelength to a value in a look-up table and delivers the associated k . This routine is used to get a reasonable first guess for k .

The second step uses Matlab's `lsqcurvefit` minimization routine with a multi-start protocol (where the code randomly generates multiple start points for all variables) to find a single k for three grain-sizes simultaneously while also solving for b , c , $\langle D \rangle$, and s within user specified bounds. `lsqcurvefit` is a least-squares minimization routine appropriate for use on non-linear equations (Coleman and Li 1994). The program finds the array of values, x , that minimizes the difference between the experimental data and the modeled data within user specified constraints. The multi-start protocol is used to ensure that global rather than local minima are obtained. Bounds for b and c were modified from Mustard and Pieters (1989), $\langle D \rangle$ was allowed to vary from $1/2$ the smallest value of the grain size range to the highest value in the grain size range, s was allowed to vary between 0.0 and $0.06 \mu\text{m}^{-1}$. Since k is, by definition, grain-size independent, this procedure provides better accuracy in solving for k than solving for each grain-size individually and then averaging them together. For this first pass, n , b , and c are considered scalars.

Once a multi grain-size k has been determined, it is used to determine a wavelength-dependent n using a singly subtractive Kramers Kronig (SSKK) transformation (Lucarini et al. 2005). For a frequency ν ,

$$n(\nu) = n_1 + \frac{(\nu^2 - \nu_1^2)}{2\pi} P \int_0^{\infty} \frac{\nu' k(\nu')}{(\nu'^2 - \nu^2)(\nu'^2 - \nu_1^2)} d\nu'. \quad (15)$$

Here, n_1 is the real index of refraction at a known point, ν_1 , and ν' is a dummy variable for integration. For n_1 , we use average literature values of n in the visible (sodium D line: 0.16970 cm^{-1} or $0.58929 \mu\text{m}$). The P in front of the integral indicates that the Cauchy principle value of the integral must be taken. Where the integral is defined, the Cauchy principle value is simply the value of the integral. When the integral diverges (as is the case when either parenthetical expression in the denominator is zero), the Cauchy principle value defined as (Mauch 2004)

$$P \int_a^b f(x) dx = \lim_{\epsilon \rightarrow 0^+} \left(\int_a^{x_0 - \epsilon} f(x) dx + \int_{x_0 + \epsilon}^b f(x) dx \right). \quad (16)$$

Since measured spectra are not continuous, but rather a collection of values at closely spaced intervals, the data are integrated by section using a Simpson's rule approximation. The code first converts wavelength to frequency and re-interpolates to an equi-spaced array (5.913 cm^{-1} spacing). Each segment is assumed to have a constant k , and the bounds of integration are set so that the known k is at the midpoint of the range. The segments are subdivided $1000\times$ to produce a 0.0059 cm^{-1} mesh, and the Simpson's rule approximation is applied. Around the singularities, the spacing is 0.003 cm^{-1} . Integration done in this way avoids adding errors encountered from the singularities. An SSKK transformation ideally requires a much larger data set than is typically available. Therefore, we used MIR k values estimated from Lorentz-Lorenz dispersion analysis (Glotch and Rossman 2009) to extend the range for a more convergent solution. If UV behavior of the material is known, data can be extended in the short wavelength

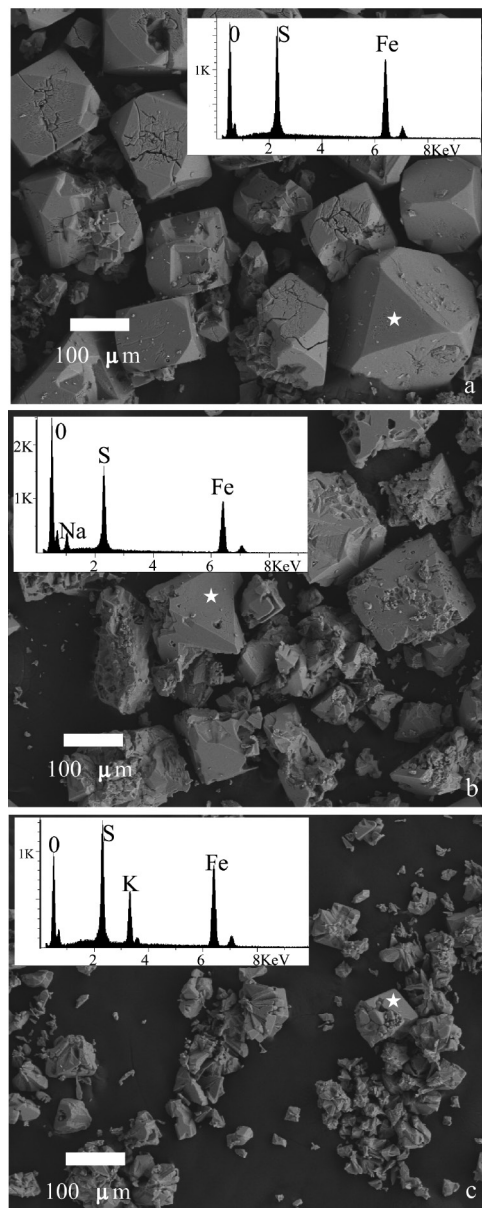


FIGURE 4. SEM images of the samples used in this study. EDS insets show the chemical composition of the point indicated. (a) hydronium jarosite, (b) sodium jarosite, and (c) potassium jarosite.

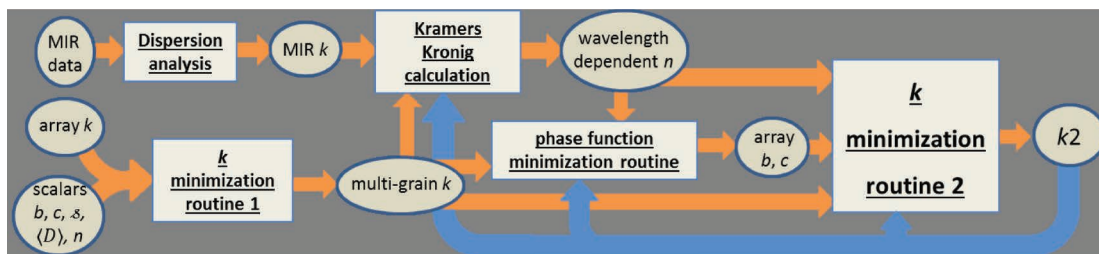


FIGURE 3. Flow chart of calculations performed by this suite of programs. The sequence starts after k has initially been determined by the lookup table program for individual grain sizes.

direction as well through linear extrapolation or curve fitting. To avoid end point problems that arise from using a finite data set, the spectra used for porosity corrected optical constants were linearly extended into the UV by 0.1 μm .

Once a wavelength-dependent n is determined, the spectra for all phase angles are run through a phase function program to determine wavelength-dependent b and c . This code also uses Matlab's lsqcurvefit program with a multistart protocol to simultaneously minimize the difference between the modeled fit and the data for all phase angles of all grain sizes. The code first creates a coarse data set (0.05 μm) spacing, and then finds a single b and c for all grain sizes and all phase angles. All phase angles of each grain size are restricted to have a single $\langle D \rangle$ and s , which are also fit during this process. The array k can be varied in this step using a scaling factor. Allowing k to vary in this way ensures that the division of the code into three parts does not overly constrain the solution for k while still maximizing the possibility of a realistic solution.

Finally, we use n , b , and c as fixed arrays to minimize for a new k using the k minimization routine, followed by the SSK routine, and then the phase function program, until values for k , n , b , and c do not vary substantially. In practice, this takes an additional two to three iterations.

RESULTS

The jarosites synthesized in this study are shown in Figure 4, and XRD analyses are shown in Figure 5. Hydronium jarosite grows as euhedral crystals with smooth faces but with deep cracks, which may propagate through the crystals. Sodium jarosite shows a great deal of pitting. Potassium jarosite seems to start as a finer-grained precipitate that then anneals to form larger grains, leading to surface roughness. Hydronium jarosite is the easiest of the three to synthesize as a coarse-grained sample, whereas sodium jarosite is the most difficult and took many attempts. The VNIR spectra for hydronium, sodium, and potassium jarosite are shown in Figures 6a, 6b, and 6c, respectively. For each sample, the coarsest size fractions have the lowest overall albedos and the finest size fractions have the highest overall albedos. This trend is consistent with what is expected for VNIR spectra of powdered minerals of different size fractions. The MIR spectra of pressed pellets of the <45 μm size fraction of each jarosite are shown in Figure 7.

Figures 8a, 8b, and 8c show the final values of wavelength-dependent variables for hydronium, sodium, and potassium jarosite, respectively. Values are reported for calculations both with and without a porosity correction. The grain-size independent imaginary index of refraction, k , for each sample

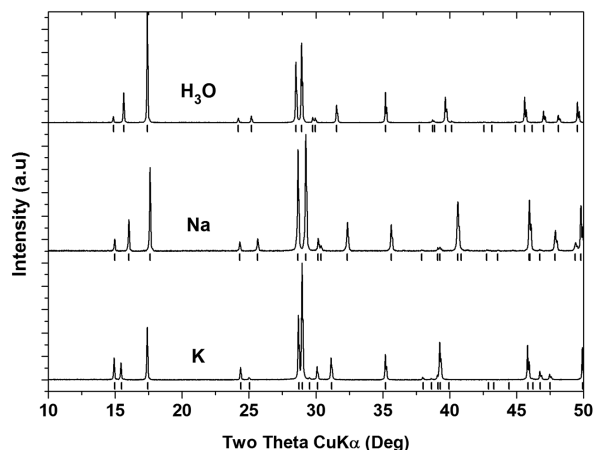


FIGURE 5. XRD patterns for hydronium (top), sodium (middle), and potassium (bottom) jarosite. Literature values are represented by ticks underneath each plot. All samples are phase pure.

is plotted at the top of each figure; the grain-size independent real index of refraction, n , is plotted in the middle of each figure; and the value of $p(g)$ vs. wavelength for $g = 30^\circ$ is plotted at the bottom of each figure. The other minimized parameters (s and $\langle D \rangle$), along with the porosity correction used for each sample, are listed in Table 1.

Figure 9 shows the modeled spectra derived from using the grain-size independent values to produce grain-size specific VNIR spectra. The modeled results are overlaid on laboratory reflectance spectra.

The MIR indices of refraction derived from the application of a Lorentz-Lorentz dispersion analysis are shown in Figure 10, and the dispersion parameters for each modeled spectrum are provided at <http://aram.ess.sunysb.edu/tglotch/spectra.html>, along with the MIR spectra and tabulated n and k values. The top pane of each plot shows the fit overlaid on the laboratory spectrum. Recall that since the MIR data were acquired from powder pressed into pellets, these values are likely off by a

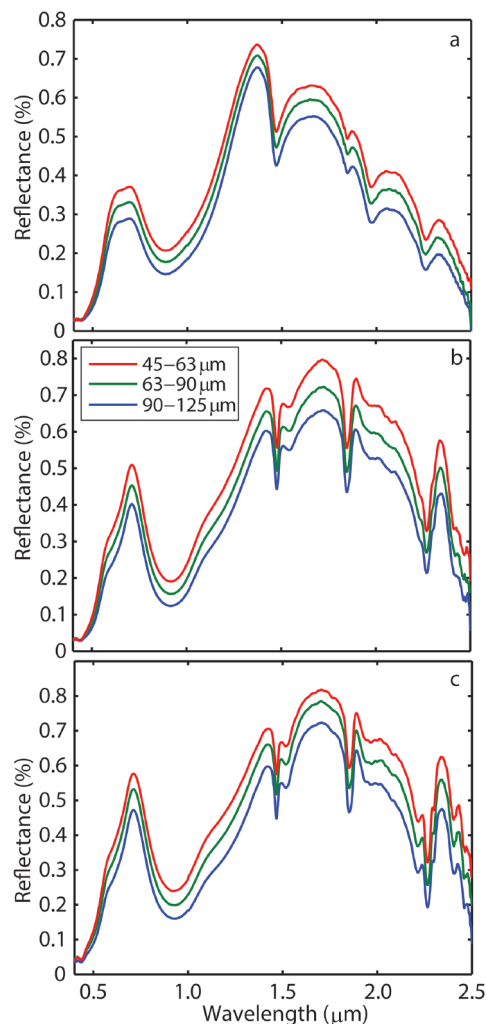


FIGURE 6. VNIR spectra of hydronium (a), sodium (b), and potassium (c) jarosite. Spectra for 45–63, 63–90, and 90–125 μm size fractions are shown for each sample.

factor of ~ 2 from those that would be modeled from polished single-crystal specimens (Pecharroman et al. 1995).

DISCUSSION

It must not be taken for granted that values obtained by this type of modeling are simply the number or numbers that create the closest numerical match between the modeled fit and the laboratory data. The goodness of fit between the model and the data are often, but not always, a sign of how well the theory represents the real system. In the case of optical constant determination, a perfect match between the model and the data can be obtained for various solutions. This is because, depending on the configuration of the code, the problem is either under-determined (not enough constraints for the number of data points) or over-determined (more constraining parameters than the number of data points). The seeming complexity of the procedure used for this study seeks to balance these two cases to maximize the probability of reaching a real and unique solution. Here, we discuss and justify these choices.

Lookup table approach

The under-determined case occurs when k is obtained from a single grain-size spectrum at a single phase angle. Here, b , c , δ , and $\langle D \rangle$, along with the array, k , are variables. This creates a system of linear equations the length of the data set (N), but with $N+4$ unknowns. Historically, the most efficient method for dealing with this problem has been to make three simplifying assumptions: first, that the surface is made up of isotropic scatterers, thus removing the phase function coefficients b and c from consideration; second, δ is fixed at near zero; and third, $\langle D \rangle$ is specified based on prior knowledge or reasonable assumptions.

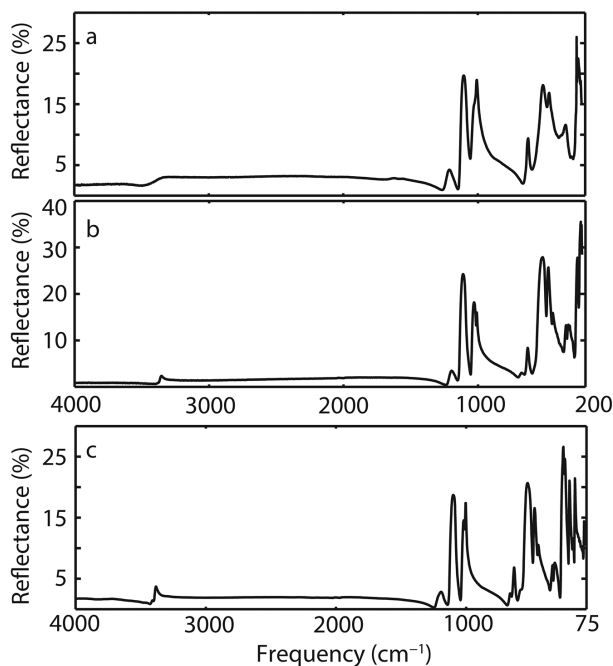


FIGURE 7. MIR data for hydronium jarosite (a) and sodium jarosite (b). MIR and FIR data for potassium jarosite (c).

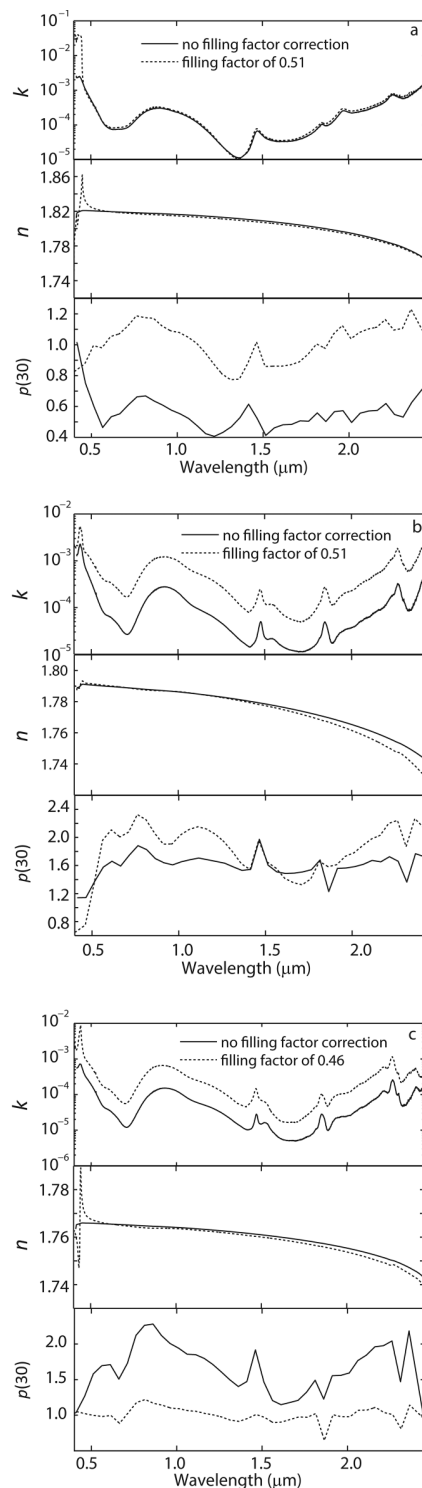


FIGURE 8. Wavelength-dependent variables for hydronium (a), sodium (b), and potassium (c) jarosite, respectively. The grain-size independent imaginary index of refraction, k , for each sample is plotted at the top, the grain-size independent real index of refraction, n , is plotted in the middle, and the value of $p(g)$ vs. wavelength for $g = 30^\circ$ is plotted at the bottom. Variables determined using a porosity correction are shown with a dashed line.

In this case, a table can be created of modeled values calculated from a range of k values over the span of wavelengths. Each data point is matched to a value in the table, thus providing a specific k for each wavelength. If we assume knowledge of b and c , a similar table can be produced for the non-isotropic case. This “lookup table” approach is, indeed, how the first approximation of k is derived.

Determining k in this fashion does not provide any means for verifying the solution. Since, however, k is a fundamental property of the material, it is, by definition, grain-size independent. Therefore, previous authors have constrained k either by averaging the k values for samples of multiple grain sizes or by adjusting $\langle D \rangle$ so that k values for multiple grain sizes fall closer to the mean (Lucy 1998; Roush et al. 2007). Minimization

TABLE 1. Values of the near-surface scattering factor, s (μm^{-1}), and the apparent grain size, $\langle D \rangle$ (μm) delivered in the final minimization for calculations both with and without a porosity correction (the value of the porosity correction is also listed)

	No porosity correction			$\phi = 0.51$		$\phi = 0.46$
	H-Jar	Na-Jar	K-Jar	H-Jar	Na-Jar	K-Jar
s 45–63	10^{-17}	0.04	10^{-14}	0.01	0.05	0.06
s 63–90	0.04	0.06	0.08	0.01	0.05	0.04
s 90–125	0.04	0.07	0.05	10^{-14}	0.03	0.03
$\langle D \rangle$ 45–63	20.5	59.8	51.0	63 ^a	42.3	57.6
$\langle D \rangle$ 63–90	26.7	89.3	72.9	79.5	58.9	76.9
$\langle D \rangle$ 90–125	35.6	125.9	112.8	103.3	77.5	110.2

^a Upper limit.

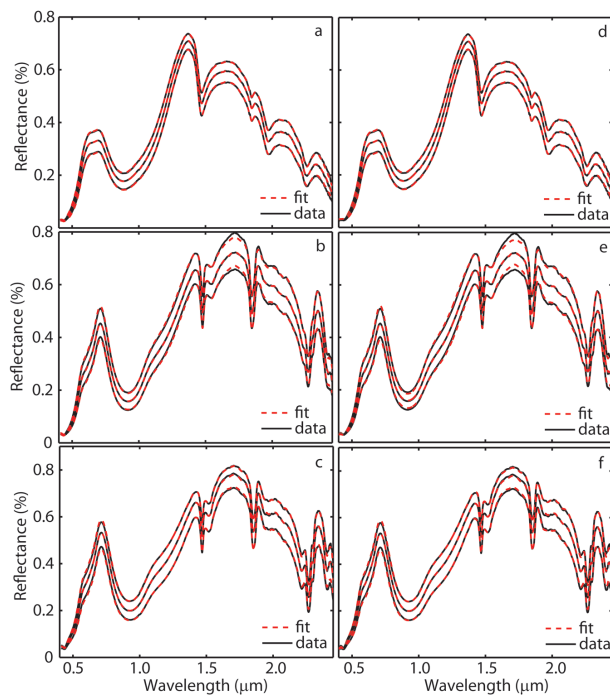


FIGURE 9. Modeled fits produced from multi-grain size k values for all three grain sizes of hydronium (a and d), sodium (b and e), and potassium (c and f) jarosite. Porosity corrections were used for d, e, and f. For each sample, the 45–63 μm spectrum is on top, the 63–90 μm spectrum is in the middle, and 90–125 μm spectrum is on the bottom.

routines, like the one used in this study, allow for the simultaneous fitting of multiple data sets to determine a single array for k . Figure 11 compares the “best fit” (minimum deviation between model and data) k obtained from the multi-minimization routine with k values obtained from “lookup tables” for both the isotropic case and the case where b and c are held fixed. Both “lookup table” k values shown are averages of the three grain sizes. Figure 11 shows that the k curve produced in the multi-minimization routine is not the same as the average of the grain-size dependent k curves for the other cases. So, while both methods attempt to create a unique solution through the use of multiple grain sizes,

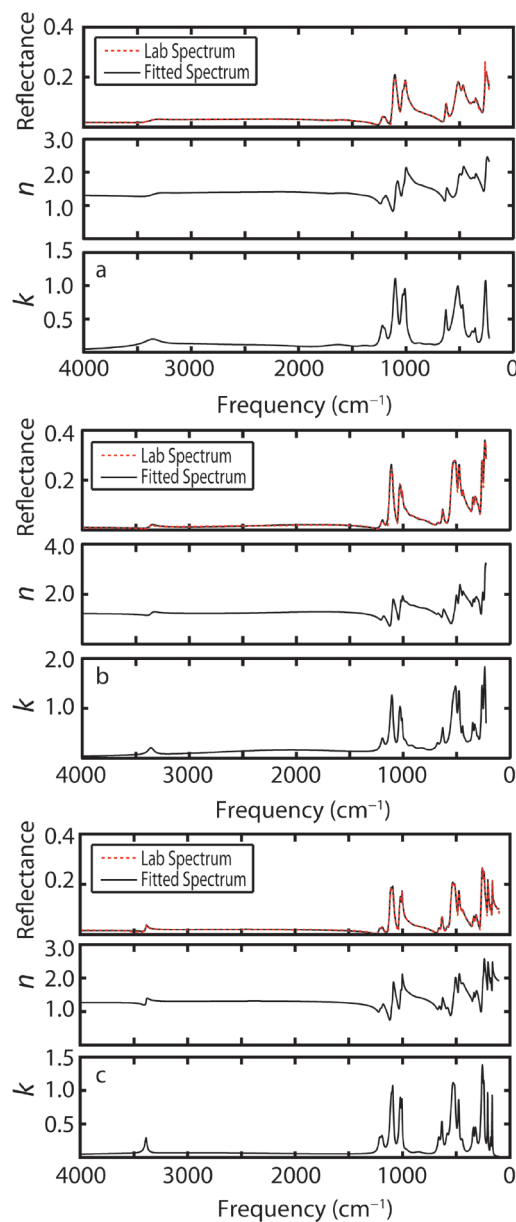


FIGURE 10. MIR optical constants for hydronium (a), sodium (b), and potassium (c) jarosite. The modeled fit for each sample is shown in the top pain with the laboratory spectrum.

the multi-minimization routine is more likely to converge closer to the true unique solution because the grain sizes constrain k during the fitting process.

Shkuratov approach

Determining k using Shkuratov's formulation (Shkuratov et al. 1999) does not suffer from this non-uniqueness problem. Since the only free parameters for the Shkuratov method are the optical constants, n and k , the porosity q and the average path length of light before reflection, S (Shkuratov et al. 1999), there can be only one solution for k for a single S and q . Actually, Shkuratov et al. (1999) found that value of k is only mildly dependent upon q , so each k is primarily dependent on S . But the parameter S in the Shkuratov model is equivalent to $\langle D \rangle$ in the Hapke model. So, k in the Shkuratov model is necessarily grain-size dependent. In other words, it is mathematically impossible for k to be the same for multiple grain sizes using that model unless it is assumed that the path-length of light in all grain sizes is the same. While it is understood by users of this model that k is, by definition, grain-size independent, final k values are typically determined by averaging multiple k values or adjusting other parameters so that k falls close to the mean (Roush et al. 2007). However, because we have found that the multi-grain size k is not the average of k values determined for the three grain sizes independently, we argue that the optical constant values determined through the Shkuratov model are useful approximations (Fig. 12), but are not the true optical constants of the material.

Phase function

Where the Shkuratov model simplifies calculations by removing dependence of k on viewing geometry, the Hapke

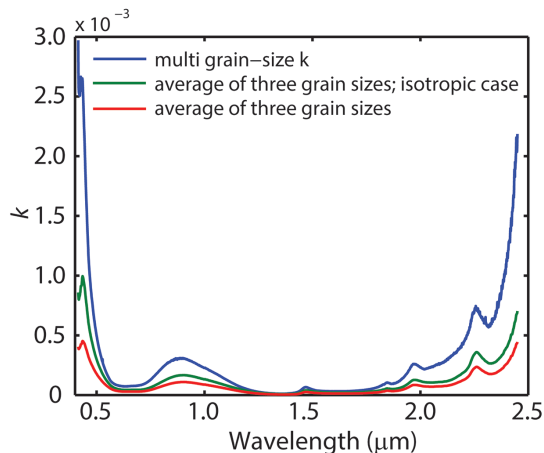


FIGURE 11. Imaginary index of refraction k , calculated for hydronium jarosite under three conditions: (1) simultaneous minimization to get a single k for three grain sizes (no porosity correction), while solving for b , c , s , and $\langle D \rangle$ (blue); (2) assuming an isotropic phase function, then using a lookup table to find k for each grain size, assuming knowledge of s and $\langle D \rangle$, and then averaging the results (green); (3) the same as the isotropic case except assuming forward scattering phase function coefficients (Mustard and Pieters 1989) (red). The three cases do not produce equivalent results for this sample.

method utilizes this dependence to further constrain the problem. Measuring each sample over a range of phase angles makes it possible to determine values for b and c . It is typical to determine a phase function at a single wavelength over a larger continuum of phase space. But since the goniometer and spectrometer used in this study produced full size data sets at each phase angle, and since Matlab's minimization routines can process large data sets, phase function coefficients were determined for the full wavelength range. Introducing an additional 3N variables, however, created a highly over-determined problem that suffered from non-uniqueness of fit.

Our initial tests showed that the phase function did not vary

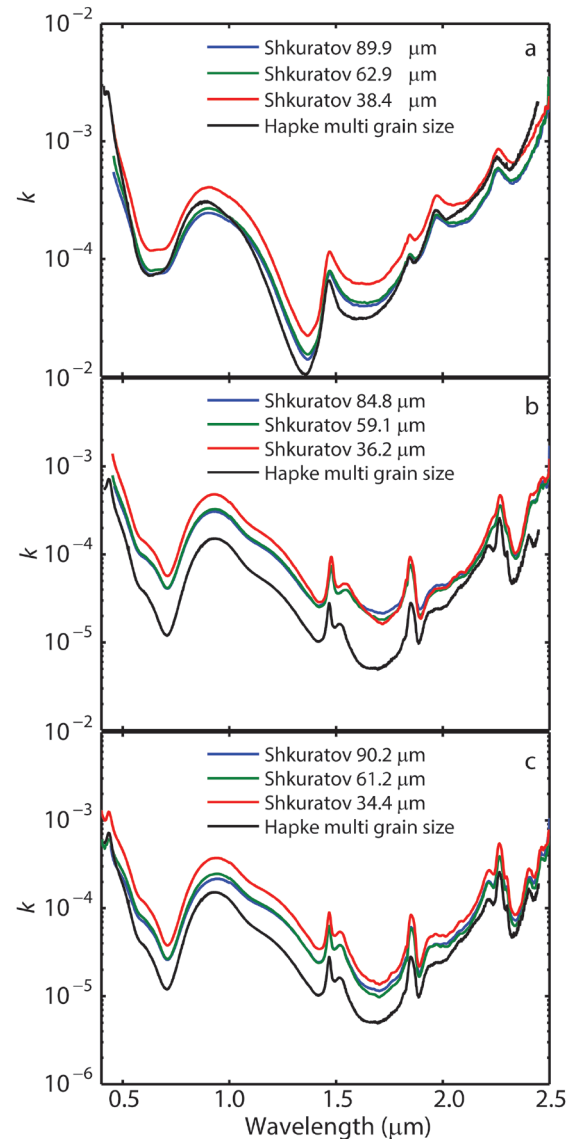


FIGURE 12. Imaginary index of refraction k determined using the Shkuratov method vs. the method described in this paper for hydronium (a), sodium (b), and potassium (c) jarosite (no porosity correction). The grain size values that produced the best fits using the Shkuratov method are listed in the legends. The final grain sizes determined using this paper's method are listed in Table 1.

systematically with grain size. Therefore, we made a simplifying assumption that the phase function is the same for all grain sizes. This leaves only s and $\langle D \rangle$ to account for spectral differences associated with grain size. This assumption also addresses the issue of over-determination. The phase function coefficients are optimized for 3 grain sizes at 7 phase angles for a total of 27 spectra to be modeled from a single phase function coefficient curve. The measured and modeled spectra for one of these fits are shown in Figure 13.

The phase function chosen for this work was a two term Legendre polynomial. Although we also investigated the use of both two and three term double Heyney-Greenstein phase functions, the Legendre polynomial provided the only reasonable fits for this system. We recommend that other investigators determine which phase function is best for each individual system as the results may vary.

Phase function data collection and the phase function minimization routine have the potential to consume large amounts of laboratory and computation time, respectively. Therefore, we tested several scaled-down procedures to determine whether equivalent results could be obtained. An ideal data set for determining the actual phase function for a mineral would contain as wide a range of phase angles as possible. What we determine in this step, however, is probably a combination of

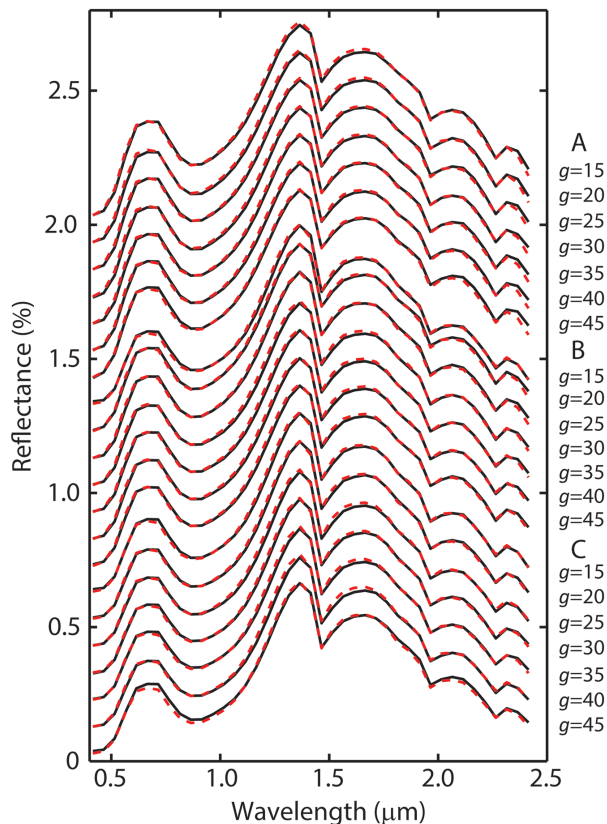


FIGURE 13. Modeled fits and laboratory spectra for hydronium jarosite's phase function minimization (no porosity correction). Spectra are offset by 0.1% for clarity. Grain size ranges are grouped, such that 90–125 μm spectra are shown in group A, 63–90 μm in group B, and 45–63 μm in group C.

phase effect, surface roughness, and shadow hiding. These effects can be explicitly accounted for using a more complicated version of Hapke's treatment (Hapke 2002). It has been shown, however, that these quantities, when solved for explicitly, do not correlate well with the physical property they are meant to describe (Shepard and Helfenstein 2007). Although a portion of the discrepancy experienced by Shepard and Helfenstein (2007) may have been due to the absence of a filling factor coefficient (Hapke, personal communication), it was the goal of this study to find the minimum number of phase angles that could reliably stabilize the results for k . A result was sought that accounted for phase, roughness, and shadow hiding, such that the value of k obtained in this study was as close to the imaginary index of refraction as possible, while still striving for the simplest experimental and theoretical configuration. We found that fewer phase angles could not produce equivalent results even when they were spaced over the same phase angle range (Fig. 14b). We determined, however, that models utilizing a down-sampled data set ($\Delta\lambda = 0.05 \mu\text{m}$) produced almost identical results to a full data set in a fraction of the computational time (Fig. 14a).

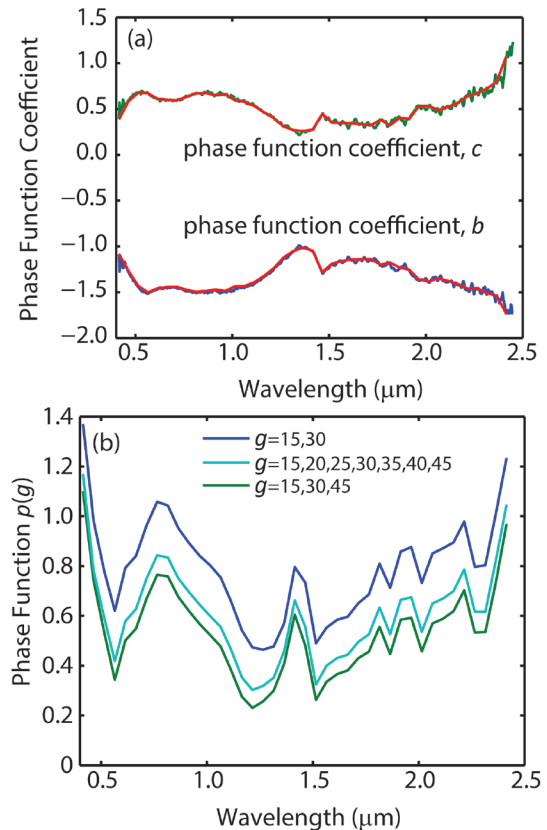


FIGURE 14. (a) $p(g)$ vs. wavelength (calculated for $g = 30^\circ$) for down-sampled data sets (red) plotted with $p(g)$ vs. wavelength (calculated for $g = 30^\circ$) for full data set. Using the full data set introduces noise over the primary features. (b) $p(g)$ vs. wavelength (calculated for $g = 30^\circ$) determined using spectra measured at $g = 15^\circ$ and $g = 30^\circ$ (blue); using spectra measured at $g = 15^\circ$, $g = 30^\circ$, and $g = 45^\circ$ data (green); and using spectra measured at $g = 15^\circ$, $g = 20^\circ$, $g = 25^\circ$, $g = 30^\circ$, $g = 35^\circ$, $g = 40^\circ$, and $g = 45^\circ$ (cyan). All grain sizes were used for all angles. The results are not equivalent. Spectral data are from hydronium jarosite.

The derived b and c values are then re-interpolated to the fine wavelength spacing.

Kramers-Kronig transformation

The wavelength range of the data set used in this study was chosen based on results for the determination of n from k using the singly subtractive Kramers-Kronig (SSKK) approach. A Kramers-Kronig transformation ideally requires a data set that spans from 0 to infinity. Since this is not possible with laboratory data, we performed a series of experiments using VNIR data and varying amounts of MIR and FIR data (extending our data set to 25, 50, 75, and 100 μm) to assess results from data sets with limited wavelength ranges. When k data for the VNIR and MIR are plotted together (Fig. 15), the difference in magnitude of the two data sets is apparent (k in the MIR is orders of magnitude greater than k in the VNIR). Therefore, it is clear that including the MIR data in the integration will have a strong influence on the result.

Figure 15 shows that there is an offset between the VNIR data and the MIR data. We adjusted the MIR data to overlap with the VNIR data using a simple linear offset plus extrapolation. The result from that procedure is shown in Figure 16. The continuous slope of the data set supports this type of correction. The corrected and combined k values were then run through the SSJK conversion, using data sets ranging from 2.5 to 50 μm (Fig. 17). The VNIR n values continue to change substantially for data sets that do not extend to at least 25 μm .

An interesting feature about the shape of n curve in the VNIR is that, when MIR data are included, the curve becomes fairly featureless throughout the NIR and slopes down toward the MIR. This trend is identical for all samples with the differences arising from the value of n at the anchor point in the VNIR. Work from other authors shows the same trend (Roush et al. 2007). This characteristic may serve as a way to approximate n in the VNIR without taking MIR data, if a predictable pattern can be determined.

Errors

The largest source of error in the computation of optical constants using the method outlined in this paper is the value of the filling factor (the porosity correction), which can change the value of k by up to a factor of 2 (Hapke 2012). Due to the uncertainty associated with the filling factor estimate, the optical constant values calculated both with and without a porosity

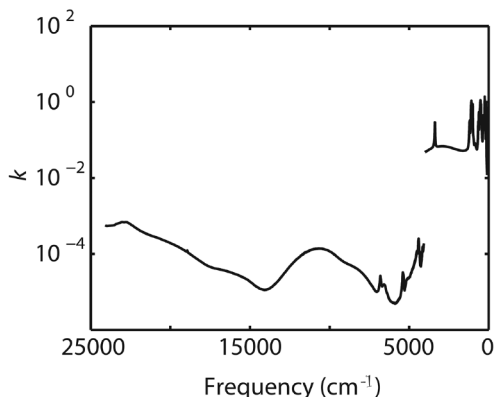


FIGURE 15. MIR and VNIR k data plotted for potassium jarosite.

correction are reported. The second largest source of error is associated with the phase angle. The errors were therefore determined by taking the same spectrum and running it through the program using phase angle g , $g+2^\circ$, and $g-2^\circ$, thus determining the variation in optical constant values that would result from misrepresentation of the phase angle. Those results for potassium jarosite (with a porosity correction) are plotted in Figure 18.

Final remarks

In the absence of large single crystals, the optical constants determined by our method are the closest approximation to the real optical constants of synthetic potassium, hydronium, and sodium jarosite that can be achieved. This leads to two questions: are synthetic samples appropriate proxies for natural samples? And are the end-member optical constants sufficient to model jarosites within the solid solution? The most common deviation between synthetic and natural jarosites is metal site occupancy (Swayze et al. 2008). The synthesis method used in this

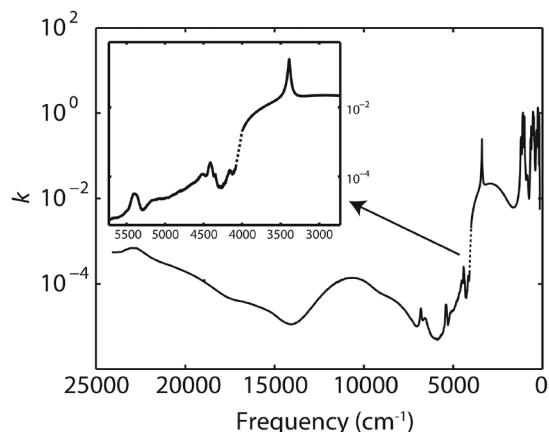


FIGURE 16. Adjusted and extrapolated k data for potassium jarosite. Note the continuity of the curve.

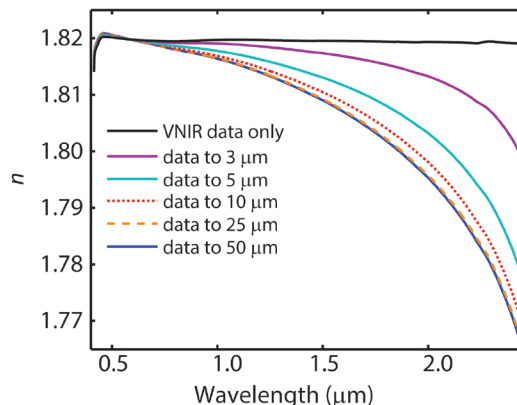


FIGURE 17. The real index of refraction n for hydronium jarosite calculated from k values that extend to 2.5, 3.0, 5.0, 10, 25, and 50 μm (no porosity correction). VNIR data only become equivalent when MIR data out to at least 25 μm are used. These calculations, performed in frequency space, may be less sensitive to MIR data than those performed in wavelength space by the same method.

study was specifically designed to eliminate metal vacancies in the lattice (Nocera et al. 2004). In addition, after studying the cell dimensions of both hydrothermal and low-temperature jarosites, Swayze et al. (2008) concluded that natural jarosites crystallize as mixtures of end-members, not as intermediate compositions in the solid-solution series. Thus, the optical constants determined in this study should be appropriate for modeling natural jarosites in all environments.

IMPLICATIONS

The use of modeling techniques that determine quantitative abundances from particulate surfaces in the VNIR has been hindered by the lack of available n and k data for many of the relevant minerals. The optical constants presented in this paper allow for the use of such modeling techniques to derive abundances of the mineral jarosite, on Earth and Mars, from mixed spectra. These abundances can be used on Mars to constrain surface processes that led to jarosite formation, and they can be used on Earth to

monitor AMD and jarosite wastes.

The detailed description of the technique used in this paper, along with the availability of our Matlab code, has the potential to greatly expand this library of data in the near future. The process outlined in this study, although based on complicated theory, requires three simple inputs: a sample in three grain sizes that can be measured at several phase angles, MIR measurements of the same sample out to 50 μm , and a desktop computer capable of running Matlab (less than two weeks computation time on a single core). All data and programs used in this study are available at <http://aram.ess.sunysb.edu/tglotch/tools.html>.

ACKNOWLEDGMENTS

We thank Ted Roush for assistance with the computer modeling of the Kramers-Kronig calculation.

The synthesis and XRD characterization work at Stony Brook was supported by the National Science Foundation (NSF) through Collaborative Research (CRC) in Chemistry Grant CHE0714183.

We thank Bruce Hapke and Samuel Lawrence for helpful insights and suggestions provided in review of this manuscript.

REFERENCES CITED

- Ambartsumian, V. (1958) The theory of radiative transfer in planetary atmospheres. In V. Ambartsumian, Ed., *Theoretical Astrophysics*, p. 550–564. Pergamon, New York.
- Barron, V., Torrent, J., and Greenwood, J.P. (2006) Transformation of jarosite to hematite in simulated Martian brines. *Earth and Planetary Science Letters*, 251, 380–385.
- Bell, J.H., Bowen, B.B., and Martini, B.A. (2010) Imaging spectroscopy of jarosite cement in the Jurassic Navajo Sandstone. *Remote Sensing of Environment*, 114, 2259–2270.
- Bigham, J.M., Schwertmann, U., and Pfab, G. (1996a) Influence of pH on mineral speciation in a bioreactor simulating acid mine drainage. *Applied Geochemistry*, 11, 845–849.
- Bigham, J.M., Schwertmann, U., Traina, S.J., Winland, R.L., and Wolf, M. (1996b) Schwertmannite and the chemical modeling of iron in acid sulfate waters. *Geochimica et Cosmochimica Acta*, 60, 2111–2121.
- Bishop, J.L., and Murad, E. (2005) The visible and infrared spectral properties of jarosite and alunite. *American Mineralogist*, 90, 1100–1107.
- Bishop, J.L., Darby Dyar, M., Lane, M.D., and Banfield, J.F. (2004) Spectral identification of hydrated sulfates on Mars and comparison with acidic environments on Earth. *International Journal of Astrobiology*, 3, 275–285.
- Cahill, J.T., and Lucey, P.G. (2007) Radiative transfer modeling of lunar highlands spectral classes and relationship to lunar samples. *Journal of Geophysical Research-Planets*, 112, E10007.
- Cahill, J.T.S., Lucey, P.G., and Wiecezorek, M.A. (2009) Compositional variations of the lunar crust: Results from radiative transfer modeling of central peak spectra. *Journal of Geophysical Research-Planets*, 114, E09001.
- Chandrasekhar, S. (1960) *Radiative Transfer*. Dover, New York.
- Clark, R.N. (1999) *Spectroscopy of rocks and minerals, and principles of spectroscopy*. In A.N. Rencz, Ed., *Manual of remote sensing*, vol 3, 3–58. Remote Sensing for the Earth Sciences, Wiley, New York.
- Clark, R.N., and Roush, T.L. (1984) Reflectance spectroscopy—Quantitative-analysis techniques for remote-sensing applications. *Journal of Geophysical Research*, 89, 6329–6340.
- Clark, R.N., Swayze, G.A., Livio, K.E., Kokaly, R.F., Sutley, S.J., Dalton, J.B., McDougal, R.R., and Gent, C.A. (2003) Imaging spectroscopy: Earth and planetary remote sensing with the USGS Tetracorder and expert systems. *Journal of Geophysical Research-Planets*, 108, 5131.
- Cloutis, E.A., Craig, M.A., Kruzelecky, R.V., Jamroz, W.R., Scott, A., Hawthorne, F.C., and Mertzman, S.A. (2008) Spectral reflectance properties of minerals exposed to simulated Mars surface conditions. *Icarus*, 195, 140–168.
- Coleman, T., and Li, Y. (1994) On the convergence of interior-reflective Newton methods for nonlinear minimization subject to bounds. *Mathematical Programming*, 67, 189–224.
- Cruikshank, D.P., Owen, T.C., Ore, C.D., Geballe, T.R., Roush, T.L., de Bergh, C., Sandford, S.A., Poulet, F., Benedix, G.K., and Emery, J.P. (2005) A spectroscopic study of the surfaces of Saturn's large satellites: H₂O ice, tholins, and minor constituents. *Icarus*, 175, 268–283.
- Dalton, J.B. III, and Pitman, K.M. (2012) Low temperature optical constants of some hydrated sulfates relevant to planetary surfaces. *Journal of Geophysical Research-Planets*, 117, E09001.
- Dalton, J.B., Bove, D.J., Mladimich, C.S., and Rockwell, B.W. (2004) Identification of spectrally similar materials using the USGS Tetracorder algorithm: the calcite-epidote-chlorite problem. *Remote Sensing of Environment*, 89, 455–466.
- Denevi, B.W., Lucey, P.G., and Sherman, S.B. (2008) Radiative transfer modeling of

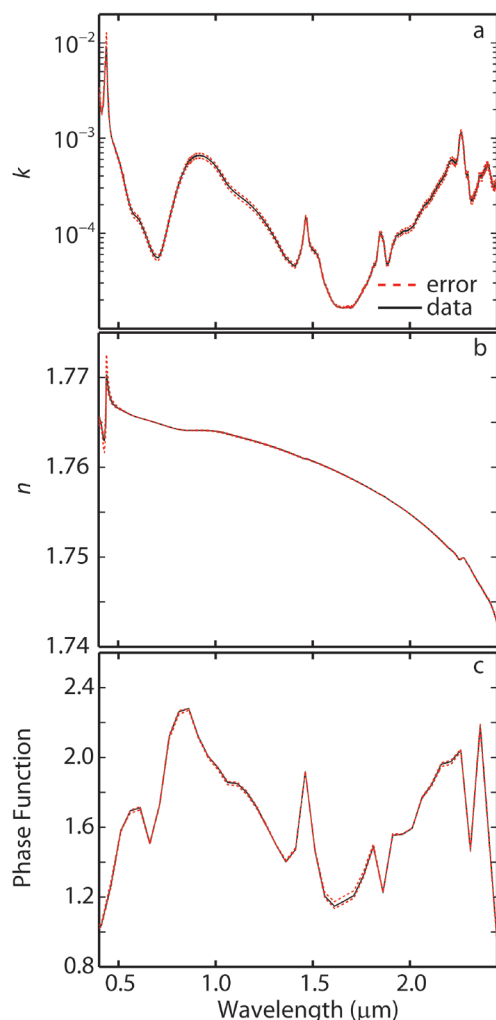


FIGURE 18. Errors associates with the wavelength-dependent variables: (a) the grain-size independent imaginary index of refraction, k ; (b) the grain-size independent real index of refraction, n ; and (c) the value of $p(g)$ vs. wavelength for $g = 30^\circ$.

- near-infrared spectra of lunar mare soils: Theory and measurement. *Journal of Geophysical Research-Planets*, 113, E02003.
- Deyell, C.L., and Dipple, G.M. (2005) Equilibrium mineral-fluid calculations and their application to the solid solution between alunite and natroalunite in the El Indio-Pascua belt of Chile and Argentina. *Chemical Geology*, 215, 219–234.
- Drouet, C., and Navrotsky, A. (2003) Synthesis, characterization, and thermochemistry of K-Na-H₂O jarosites. *Geochimica et Cosmochimica Acta*, 67, 2063–2076.
- Farrand, W.H., Glotch, T.D., Rice, J.W., Huroowitz, J.A., and Swayze, G.A. (2009) Discovery of jarosite within the Mawrth Vallis region of Mars: Implications for the geologic history of the region. *Icarus*, 204, 478–488.
- Frost, R.L., Wills, R.A., Martens, W., and Weier, M. (2005) NIR spectroscopy of jarosites. *Spectrochimica Acta Part a-Molecular and Biomolecular Spectroscopy*, 62, 869–874.
- Glotch, T.D., and Rossman, G.R. (2009) Mid-infrared reflectance spectra and optical constants of six iron oxide/oxyhydroxide phases. *Icarus*, 204, 663–671.
- Grohol, D., Nocera, D.G., and Papoutsakis, D. (2003) Magnetism of pure iron jarosites. *Physical Review B*, 67, 064401.
- Hapke, B. (1981) Bidirectional reflectance spectroscopy 1. Theory. *Journal of Geophysical Research*, 86, 3039–3054.
- (1993) Theory of reflectance and emittance spectroscopy. *Topics in Remote Sensing* 3, 455 p. Cambridge University Press, New York.
- (1996) A model of radiative and conductive energy transfer in planetary regoliths. *Journal of Geophysical Research-Planets*, 101, 16817–16831.
- (2002) Bidirectional reflectance spectroscopy 5. The coherent backscatter opposition effect and anisotropic scattering. *Icarus*, 157, 523–534.
- (2008) Bidirectional reflectance spectroscopy 6. Effects of porosity. *Icarus*, 195, 918–926.
- (2012) Theory of reflectance and emittance spectroscopy, 2nd ed., 513 p. Cambridge University Press, New York.
- Hapke, B., and Wells, E. (1981) Bidirectional reflectance spectroscopy 2. Experiments and observations. *Journal of Geophysical Research*, 86, 3055–3060.
- Jerz, J.K., and Rimstidt, J.D. (2003) Efflorescent iron sulfate minerals: Paragenesis, relative stability, and environmental impact. *American Mineralogist*, 88, 1919–1932.
- Klingelhofer, G., Morris, R.V., Bernhardt, B., Schroder, C., Rodionov, D.S., de Souza, P.A., Yen, A., Gellert, R., Evlanov, E.N., Zubkov, B., and others. (2004) Jarosite and hematite at Meridiani Planum from Opportunity's Mossbauer spectrometer. *Science*, 306, 1740–1745.
- Kula, J., and Baldwin, S.L. (2011) Jarosite, argon diffusion, and dating aqueous mineralization on Earth and Mars. *Earth and Planetary Science Letters*, 310, 314–318.
- Lawrence, S.J., and Lucey, P.G. (2007) Radiative transfer mixing models of meteoritic assemblages. *Journal of Geophysical Research-Planets*, 112, E07005.
- Li, S., and Li, L. (2011) Radiative transfer modeling for quantifying lunar surface minerals, particle size, and submicroscopic metallic Fe. *Journal of Geophysical Research-Planets*, 116, E09001.
- Lucarini, V., Saarinen, J.J., Peiponen, K.-E., and Vartiainen, E.M. (2005) *Kramers-Kronig Relations in Optical Materials Research*. Springer Series in Optical Sciences. Springer, New York, 162 pp.
- Lucey, P.G. (1998) Model near-infrared optical constants of olivine and pyroxene as a function of iron content. *Journal of Geophysical Research-Planets*, 103, 1703–1713.
- (2004) Mineral maps of the Moon. *Geophysical Research Letters*, 31, L08701.
- Lueth, V.W., Rye, R.O., and Peters, L. (2005) "Sour gas" hydrothermal jarosite: Ancient to modern acid-sulfate mineralization in the southern Rio Grande Rift. *Chemical Geology*, 215, 339–360.
- Madden, M.E.E., Bodnar, R.J., and Rimstidt, J.D. (2004) Jarosite as an indicator of water-limited chemical weathering on Mars. *Nature*, 431, 821–823.
- Madden, M.E.E., Guess, J.R., Madden, A.S., and Rimstidt, J.D. (2008) Measuring jarosite dissolution rates to determine jarosite lifetimes on Earth and Mars. *Geochimica et Cosmochimica Acta*, 72, A243–A243.
- Madden, M.E.E., Madden, A.S., and Rimstidt, J.D. (2009) How long was Meridiani Planum wet? Applying a jarosite stopwatch to determine the duration of aqueous diagenesis. *Geology*, 37, 635–638.
- Madden, M.E.E., Madden, A.S., Rimstidt, J.D., Zahrai, S., Kendall, M.R., and Miller, M.A. (2012) Jarosite dissolution rates and nanoscale mineralogy. *Geochimica et Cosmochimica Acta*, 91, 306–321.
- Majzlan, J., Stevens, R., Boerio-Goates, J., Woodfield, B.F., Navrotsky, A., Burns, P.C., Crawford, M.K., and Amos, T.G. (2004) Thermodynamic properties, low-temperature heat-capacity anomalies, and single-crystal X-ray refinement of hydronium jarosite, (H₃O)Fe₃(SO₄)₂(OH)₆. *Physics and Chemistry of Minerals*, 31, 518–531.
- Mauch, S. (2004) Introduction to Methods of applied mathematics or advanced mathematical methods for scientists and engineers. <http://www.its.caltech.edu/~sean>.
- Mustard, J.F., and Pieters, C.M. (1987) Quantitative abundance estimates from bidirectional reflectance measurements. *Journal of Geophysical Research-Solid Earth and Planets*, 92, E617–E626.
- (1989) Photometric phase function of common geological minerals and applications to quantitative-analysis of mineral mixture reflectance spectra. *Journal of Geophysical Research-Solid Earth and Planets*, 94, 13619–13634.
- Navrotsky, A., Forray, F.L., and Drouet, C. (2005) Jarosite stability on Mars. *Icarus*, 176, 250–253.
- Nocera, D.G., Bartlett, B.M., Grohol, D., Papoutsakis, D., and Shores, M.P. (2004) Spin frustration in 2D kagome lattices: A problem for inorganic synthetic chemistry. *Chemistry—A European Journal*, 10, 3851–3859.
- Nomura, K., Takeda, M., Iiyama, T., and Sakai, H. (2005) Mossbauer studies of jarosite, mikasaite and yavapaiite, and implication to their Martian counterparts. *Hyperfine Interactions*, 166, 657–664.
- Norlund, K.L.L., Baron, C., and Warren, L.A. (2010) Jarosite formation by an AMD sulphide-oxidizing environmental enrichment: Implications for biomarkers on Mars. *Chemical Geology*, 275, 235–242.
- Papike, J.J., Karter, J.M., and Shearer, C.K. (2006) Comparative planetary mineralogy: Implications of martian and terrestrial jarosite. A crystal chemical perspective. *Geochimica et Cosmochimica Acta*, 70, 1309–1321.
- Papike, J.J., Burger, P.V., Karter, J.M., Shearer, C.K., and Lueth, V.W. (2007) Terrestrial analogs of martian jarosites: Major, minor element systematics and Na-K zoning in selected samples. *American Mineralogist*, 92, 444–447.
- Pappu, A., Savena, M., and Asolekar, S.R. (2006) Jarosite characteristics and its utilisation potentials. *Science of the Total Environment*, 359, 232–243.
- Pecharroman, C., Gonzalezcarreno, T., and Iglesias, J.E. (1995) The infrared dielectric-properties of maghemite, gamma-Fe₂O₃, from reflectance measurement on presses powders. *Physics and Chemistry of Minerals*, 22, 21–29.
- Piatek, J.L. (2003) Size-dependent scattering properties of planetary regolith analogs, 186 p. Ph.D. thesis, University of Pittsburgh, Pennsylvania.
- Poulet, F., and Erard, S. (2004) Nonlinear spectral mixing: Quantitative analysis of laboratory mineral mixtures. *Journal of Geophysical Research-Planets*, 109, E02009.
- Poulet, F., Bibring, J.P., Langevin, Y., Mustard, J.F., Mangold, N., Vincendon, M., Gondet, B., Pinet, P., Bardintzeff, J.M., and Platevoet, B. (2009) Quantitative compositional analysis of martian mafic regions using the MEx/OMEGA reflectance data. *Icarus*, 201, 69–83.
- Pritchett, B.N., Madden, M.E.E., and Madden, A.S. (2012) Jarosite dissolution rates and maximum lifetimes in high salinity brines: Implications for Earth and Mars. *Earth and Planetary Science Letters*, 357, 327–336.
- Quinn, D. (2010) The Hapke Model in Excel. <http://davenquinn.com/hapke/>.
- Quinn, D.P., Gillis-Davis, J.J., and Lucey, P.G. (2010) Using Microsoft Excel for Hapke modeling: A technique to simplify calculations of optical constants and reflectance spectra. Abstracts of Papers Submitted to the Lunar and Planetary Science Conference XXXXI, The Woodlands, Texas.
- Roach, L.H., Mustard, J.F., Swayze, G., Milliken, R.E., Bishop, J.L., Murchie, S.L., and Lichtenberg, K. (2010) Hydrated mineral stratigraphy of Ius Chasma, Valles Marineris. *Icarus*, 206, 253–268.
- Roush, T.L., Esposito, F., Rossman, G.R., and Colangeli, L. (2007) Estimated optical constants of gypsum in the regions of weak absorptions: Application of scattering theories and comparisons to independent measurements. *Journal of Geophysical Research-Planets*, 112, E10003.
- Rye, R.O., and Stoffregen, R.E. (1995) Jarosite-water oxygen and hydrogen isotope fractionations: Preliminary experimental data. *Economic Geology and the Bulletin of the Society of Economic Geologists*, 90, 2336–2342.
- Sefton-Nash, E., Catling, D.C., Wood, S.E., Grindrod, P.M., and Teanby, N.A. (2012) Topographic, spectral and thermal inertia analysis of interior layered deposits in Iani Chaos, Mars. *Icarus*, 221, 20–42.
- Shepard, M.K., and Helfenstein, P. (2007) A test of the Hapke photometric model. *Journal of Geophysical Research-Planets*, 112, E03001.
- Shkuratov, Y., Starukhina, L., Hoffmann, H., and Arnold, G. (1999) A model of spectral albedo of particulate surfaces: Implications for optical properties of the moon. *Icarus*, 137, 235–246.
- Sowe, M., Wendt, L., McGuire, P.C., and Neukum, G. (2012) Hydrated minerals in the deposits of Aureum Chaos. *Icarus*, 218, 406–419.
- Swayze, G.A., Desborough, K.S., Smith, K.S., Lowers, H.A., Hammarstrom, J.M., Diehl, S.F., Leinz, R.W., and Driscoll, R.L. (2008) Understanding jarosite—from mine waste to Mars. In P.L. Verplanck, Ed., *Understanding Contaminants*, p. 8–13. U.S. Geological Survey Circular, 1328.
- Swayze, G.A., Smith, K.S., Clark, R.N., Sutley, S.J., Pearson, R.M., Vance, J.S., Hageman, P.L., Briggs, P.H., Meier, A.L., Singleton, M.J., and Roth, S. (2000) Using imaging spectroscopy to map acidic mine waste. *Environmental Science and Technology*, 34, 47–54.
- Wendt, L., Gross, C., Kneissl, T., Sowe, M., Combe, J.-P., LeDeit, L., McGuire, P.C., and Neukum, G. (2011) Sulfates and iron oxides in Ophir Chasma, Mars, based on OMEGA and CRISM observations. *Icarus*, 213, 86–103.
- Wilcox, B.B., Lucey, P.G., and Hawke, B.R. (2006) Radiative transfer modeling of compositions of lunar pyroclastic deposits. *Journal of Geophysical Research-Planets*, 111, E09001.
- Zahrai, S.K., Madden, M.E.E., Madden, A.S., and Rimstidt, J.D. (2013) Na-jarosite dissolution rates: The effect of mineral composition on jarosite lifetimes. *Icarus*, 223, 438–443.